

RESEARCH ARTICLE

10.1002/2016JB013114

Key Points:

- Transient postseismic deformation can be observed following the El Mayor-Cucapah earthquake at epicentral distances of up to 400 km
- Near-field postseismic deformation exhibits early transience that decays to a sustained rate which is elevated above the preseismic trend
- Far-field postseismic deformation can be explained with a Zener or Burgers rheology upper mantle

Supporting Information:

- Supporting Information S1

Correspondence to:

T. T. Hines,
hines@umich.edu

Citation:

Hines, T. T., and E. A. Hetland (2016), Rheologic constraints on the upper mantle from 5 years of postseismic deformation following the El Mayor-Cucapah earthquake, *J. Geophys. Res. Solid Earth*, 121, 6809–6827, doi:10.1002/2016JB013114.

Received 22 APR 2016

Accepted 13 AUG 2016

Accepted article online 18 AUG 2016

Published online 5 SEP 2016

Rheologic constraints on the upper mantle from 5 years of postseismic deformation following the El Mayor-Cucapah earthquake

T. T. Hines¹ and E. A. Hetland¹¹Department of Earth and Environmental Sciences, University of Michigan, Ann Arbor, Michigan, USA

Abstract We analyze five years of Southern California GPS data following the $M_w = 7.2$ El Mayor-Cucapah earthquake. We observe transient postseismic deformation which persists for 3 years at epicentral distances greater than ~ 200 km. In the near field, rapid postseismic transience decays to a sustained rate which exceeds its preseismic trend. We attempt to determine the mechanisms driving this deformation, where we consider afterslip at seismogenic depths and viscoelastic relaxation in the lower crust and upper mantle as candidate mechanisms. We find that early, rapid, near-field deformation can be explained with afterslip on the fault that ruptured coseismically. The later, sustained, near-field deformation can be explained with viscoelastic relaxation in the lower crust with a steady-state viscosity of $\sim 10^{19}$ Pa s and possibly continued afterslip. The later postseismic deformation in the far field is best explained with a transient viscosity of $\sim 10^{18}$ Pa s in the upper mantle. We argue that a transient rheology in the mantle is preferable over a Maxwell rheology because it better predicts the decay in postseismic deformation and also because it does not conflict with the generally higher, steady-state viscosities inferred from studies of geophysical processes occurring over longer timescales.

1. Introduction

Ground deformation in the years following a large ($M_w \gtrsim 7$) earthquake can be used to gain insight into the mechanical behavior of the crust and upper mantle. The interpretations of postseismic deformation are not always conclusive because multiple postseismic deformation mechanisms, such as afterslip or viscoelastic relaxation in the lower crust and upper mantle, can have qualitatively similar surface expressions [e.g., *Savage, 1990*]. This nonuniqueness complication can potentially be remedied if the postseismic deformation occurs in an area that is sufficiently well instrumented with GPS stations [*Hearn, 2003*]. Owing to the dense geodetic network deployed throughout the 2000s as part of the Plate Boundary Observatory, the postseismic deformation following the 4 April 2010, $M_w = 7.2$ El Mayor-Cucapah earthquake in Baja California was observed at more GPS stations than any other earthquake in California to date (see *Hauksson et al. [2011]* and *Fletcher et al. [2014]* for a detailed description of this earthquake and its seismotectonic context). With such a large collection of data, we attempt to discern the mechanisms driving the postseismic deformation.

Previous studies which have modeled postseismic deformation following the El Mayor-Cucapah earthquake include *Pollitz et al. [2012]*, *Gonzalez-Ortega et al. [2014]*, *Spinler et al. [2015]*, and *Rollins et al. [2015]*. Of these studies, *Gonzalez-Ortega et al. [2014]* and *Rollins et al. [2015]* have attempted to describe the postseismic deformation with afterslip in an elastic half-space. *Gonzalez-Ortega et al. [2014]* described 5 months of postseismic deformation, observed by interferometric synthetic aperture radar and GPS stations within ~ 50 km of the rupture, with afterslip and contraction on the coseismically ruptured fault. *Gonzalez-Ortega et al. [2014]* noted that their preferred model underestimated the GPS displacements for stations $\gtrsim 25$ km from the rupture and suggested that it could be the result of unmodeled viscoelastic relaxation. Using only continuous GPS stations, which are mostly north of the rupture zone, *Rollins et al. [2015]* found that 3 years of postseismic deformation can be adequately explained by afterslip, albeit with an implausibly large amount of slip inferred on the least constrained, southernmost fault segment. Here we suggest that the afterslip inferred by *Rollins et al. [2015]* may have been acting as a proxy for distributed relaxation in the upper mantle.

Pollitz et al. [2012], *Rollins et al. [2015]*, and *Spinler et al. [2015]* explored viscoelastic relaxation in the lower crust and upper mantle as a potential postseismic deformation mechanism. The rheology of the crust and mantle

is largely unknown, and so modeling postseismic deformation with viscoelastic relaxation requires one to assume a rheologic model and then find the best fitting rheologic parameters. The inference of these rheologic parameters is a computationally expensive nonlinear inverse problem which is typically approached with a forward modeling grid search method. Consequently, a simplified structure for the Earth must be assumed in order to minimize the number of rheologic parameters that need to be estimated. For example, it is commonly assumed that the lower crust and upper mantle are homogeneous, Maxwell viscoelastic layers, which may be too simplistic for postseismic studies [Riva and Govers, 2009; Hines and Hetland, 2013]. To further reduce the dimensions of the model space, it is also necessary to make simplifying assumptions about the behavior of afterslip. For example, one can assume a frictional model for afterslip and parametrize afterslip in terms of the unknown rheologic properties of the fault [e.g., Johnson *et al.*, 2009; Johnson and Segall, 2004]. One can also assume that afterslip does not persist for more than a few months and then model the later postseismic deformation assuming it to be the result of only viscoelastic relaxation [e.g., Pollitz *et al.*, 2012; Spinler *et al.*, 2015]. However, afterslip in similar tectonic settings has been observed to persist for decades following earthquakes [Çakir *et al.*, 2012; Cetin *et al.*, 2014]. Indeed, the preferred viscoelastic model from Pollitz *et al.* [2012] significantly underestimates deformation in the Imperial Valley, which could be indicative of unmodeled continued afterslip. Neglecting to allow for sustained afterslip as a postseismic mechanism could then lead to biased inferences of viscosities.

In this study, we perform a kinematic inversion for fault slip, allowing it to persist throughout the postseismic period while simultaneously estimating the viscosity of the lower crust and upper mantle. We create an initial model of the fault slip and effective viscosity necessary to describe early postseismic deformation using the method described in Hines and Hetland [2016]. This method uses a first-order approximation of surface deformation resulting from viscoelastic relaxation which is only applicable to the early postseismic period. In this case, our initial model describes the first 0.8 year of postseismic deformation following the El Mayor-Cucapah earthquake. We then use the inferred effective viscosity structure from the initial model to create a suite of postseismic models which we test against the 5 years of postseismic data available to date. Of the suite of models tested, we find that postseismic deformation following the El Mayor-Cucapah earthquake can be explained with a combination of afterslip on a fault segment running through the Sierra Cucapah and viscoelastic relaxation in a Zener rheology upper mantle with a transient viscosity on the order of 10^{18} Pa s.

2. Data Processing

We use continuous GPS position time series provided by University Navstar Consortium (UNAVCO) for stations within a 400 km radius about the El Mayor-Cucapah epicenter. We collectively describe the coseismic and postseismic displacements resulting from the El Mayor-Cucapah earthquake as $u_{\text{post}}(t)$. We consider the GPS position time series, $u_{\text{obs}}(t)$, to be the combination of $u_{\text{post}}(t)$, secular tectonic deformation, annual and semiannual oscillations, and coseismic offsets from significant earthquakes over the time span of this study. The 14 June 2010, $M_w = 5.8$ Ocotillo earthquake and the Brawley swarm, which included an $M_w = 5.5$ and an $M_w = 5.4$ events on 26 August 2012 (Figure 1), are the only earthquakes that produced noticeable displacements in any of the time series. We treat the displacements resulting from the Brawley swarm as a single event because the daily solutions provided by UNAVCO cannot resolve the separate events. Although the Ocotillo earthquake had its own series of aftershocks [Hauksson *et al.*, 2011], neither the Ocotillo earthquake nor the Brawley swarm produced detectable postseismic deformation. We model displacements resulting from these events with only a Heaviside function, $H(t)$, describing the coseismic offsets. We then model $u_{\text{obs}}(t)$ as

$$u_{\text{obs}}(t) = u_{\text{pred}}(t) + \epsilon, \quad (1)$$

where

$$u_{\text{pred}}(t) = u_{\text{post}}(t)H(t - t_{\text{emc}}) + c_0 + c_1 t + c_2 \sin(2\pi t) + c_3 \cos(2\pi t) + c_4 \sin(4\pi t) + c_5 \cos(4\pi t) + c_6 H(t - t_{\text{oc}}) + c_7 H(t - t_{\text{bs}}). \quad (2)$$

In the above equations, t_{emc} , t_{oc} , and t_{bs} are the times of the El Mayor-Cucapah earthquake, Ocotillo earthquake, and the Brawley swarm, respectively, c_0 through c_7 are unknown coefficients, and ϵ is the observation noise. We are using years as our unit of time which makes c_2 through c_5 the coefficients for annual and semiannual oscillations. We only estimate jumps associated with the Ocotillo earthquake and Brawley swarm for stations within 40 km of their epicenters.

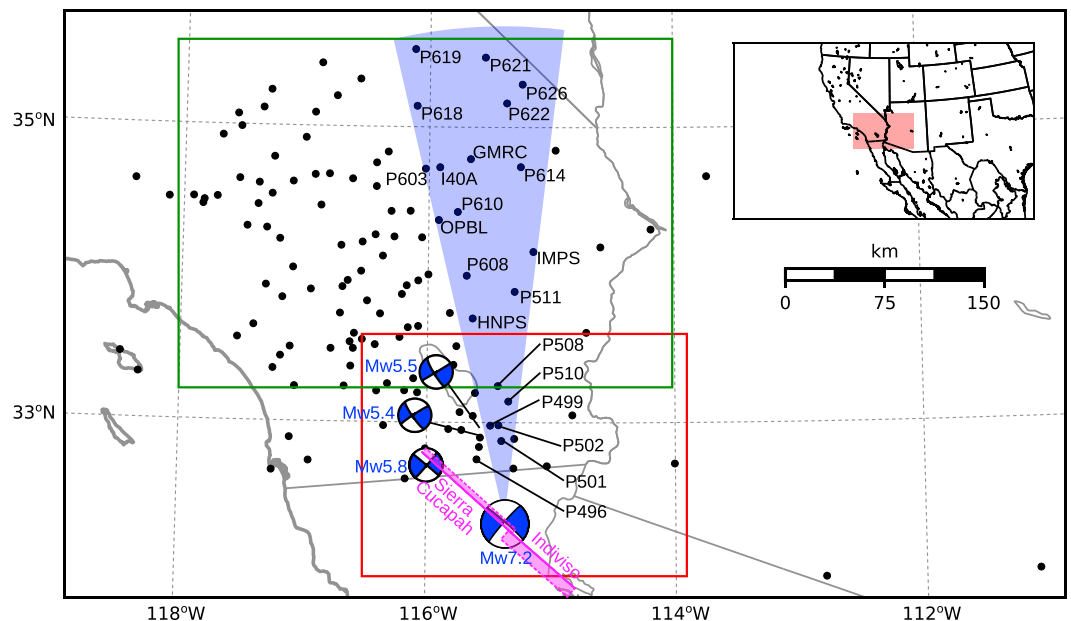


Figure 1. Map of the region considered in this study. The large focal mechanism is the Global Centroid Moment Tensor solution for the El Mayor-Cucupah earthquake, and the three small focal mechanisms are for the Ocotillo earthquake and the two main shocks during the Brawley swarm. The black dots indicate the locations of GPS stations used in this study. The fault geometry used in this study is shown in magenta where dashed lines indicate buried edges of the fault segments. The green and red boxes demarcate the extent of the near-field and far-field maps (Figures 4 and 5). Stations inside the blue sector, which highlights the area within 10° of the El Mayor-Cucupah *P* axis, are used in Figures 7 and 10.

Stations which recorded displacements that clearly cannot be described by the aforementioned processes are not included in our analysis. This includes stations in the Los Angeles Basin, where anthropogenic deformation can be larger than the postseismic signal that we are trying to estimate [Bawden *et al.*, 2001; Argus *et al.*, 2005]. In order to ensure an accurate estimation of the secular deformation, we only use stations that were installed at least 6 months prior to El Mayor-Cucupah earthquake even though several GPS stations were installed after the earthquake to get better coverage of the postseismic deformation field [Spinler *et al.*, 2015]. It would be possible to subtract secular velocities derived from elastic block models [e.g., Meade and Hager, 2005] from velocities recorded at the newly installed stations to get an estimate of postseismic velocities at those stations. However, estimating velocities from an already noisy displacement time series can introduce significant uncertainties depending on exactly how the estimation is done. We therefore use coseismic and postseismic displacements, rather than velocities, in our inverse method described in section 3. This choice prevents us from using the newly installed stations for our analysis.

The 16 October 1999, $M_w = 7.1$ Hector Mine earthquake, which occurred ~270 km north of the El Mayor-Cucupah epicenter, produced transient postseismic deformation which we do not wish to model, either mechanically or through empirical line fitting. We thus restrict our analysis to deformation observed 6 years after the Hector Mine earthquake, which is when postseismic velocities at sites near the Hector Mine epicenter are approximately constant [Savage and Svarc, 2009]. When appraising our model fit in section 3, we see some systematic residuals in the vicinity of the Hector Mine epicenter, which may be the result of errors in the assumption that the trend in Hector Mine postseismic deformation is linear after 6 years.

Studies of postseismic deformation typically assume a parametric form for $u_{\text{post}}(t)$, such as one with a logarithmic or exponential time dependence [e.g., Savage *et al.*, 2005]. However, by assuming a logarithmic or exponential form of $u_{\text{post}}(t)$, we run the risk of overfitting the GPS time series and inferring a nonexistent postseismic signal. We therefore do not assume any parametric form for $u_{\text{post}}(t)$ and rather treat it as integrated Brownian motion, so that

$$\dot{u}_{\text{post}}(t) = \sigma^2 \int_0^t w(\tau) d\tau, \quad (3)$$

where $w(t)$ is white noise and the variance of $\dot{u}_{\text{post}}(t)$ increases linearly with time by a factor of σ^2 . We use a Kalman filtering approach to estimate $u_{\text{post}}(t)$ and the unknown parameters in equation (2). In the context of Kalman filtering, our time-varying state vector is

$$\mathbf{X}(t) = [u_{\text{post}}(t), \dot{u}_{\text{post}}(t), c_0, \dots, c_7] \quad (4)$$

and equation (2) is the observation function which maps the state vector to the GPS observations. We initiate the Kalman filter by assuming a prior estimate of $\mathbf{X}(t)$ at the first time epoch, denoted $\mathbf{X}_{1|0}$, which has a sufficiently large covariance, denoted $\Sigma_{1|0}$, to effectively make our prior uninformed. For each time epoch, t_i , Bayesian linear regression is used to incorporate GPS-derived estimates of displacement with our prior estimate of the state, $\mathbf{X}_{i|i-1}$, to form a posterior estimate of the state, $\mathbf{X}_{i|i}$, which has covariance $\Sigma_{i|i}$. We then use the posterior estimate of the state at time t_i to form a prior estimate of the state at time t_{i+1} through the transition function

$$\mathbf{X}_{i+1|i} = \mathbf{F}_{i+1} \mathbf{X}_{i|i} + \delta_{i+1}, \quad (5)$$

where

$$\mathbf{F}_{i+1} = \begin{bmatrix} 1 & (t_{i+1} - t_i) & \mathbf{0} \\ 0 & 1 & \mathbf{0} \\ \mathbf{0} & \mathbf{0} & \mathbf{I} \end{bmatrix} \quad (6)$$

and δ_{i+1} is the process noise, which has zero mean and covariance described by

$$\mathbf{Q}_{i+1} = \sigma^2 \begin{bmatrix} \frac{(t_{i+1}-t_i)^3}{3} & \frac{(t_{i+1}-t_i)^2}{2} & \mathbf{0} \\ \frac{(t_{i+1}-t_i)^2}{2} & (t_{i+1} - t_i) & \mathbf{0} \\ \mathbf{0} & \mathbf{0} & \mathbf{0} \end{bmatrix}. \quad (7)$$

The covariance of the new prior state, $\mathbf{X}_{i+1|i}$, is then described by

$$\Sigma_{i+1|i} = \mathbf{F}_{i+1} \Sigma_{i|i} \mathbf{F}_{i+1}^T + \mathbf{Q}_{i+1}. \quad (8)$$

This process is repeated for each of the N time epochs. We then use Rauch-Tung-Striebel smoothing [Rauch *et al.*, 1965] to find $\mathbf{X}_{i|N}$, which is an estimate of the state at time t_i that incorporates GPS observation for all N time epochs. Our final estimates of $u_{\text{post}}(t)$ are used in subsequent analysis, while the remaining components of the state vector are considered nuisance parameters. In the interests of computational tractability, we downsample our smoothed time series from daily solutions down to weekly solutions.

The smoothness of $u_{\text{post}}(t)$ is controlled by the chosen value of σ^2 , which describes how rapidly we expect postseismic displacements to vary over time. Setting σ^2 equal to zero will effectively result in modeling $u_{\text{post}}(t)$ as a straight line which is insufficient to describe the expected transient behavior in postseismic deformation. The other end-member, where σ^2 is infinitely large, will result in $u_{\text{pred}}(t)$ overfitting the data. While one can use a maximum likelihood-based approach for picking σ^2 [e.g., Segall and Mathews, 1997], we instead take a subjective approach and choose a value for σ^2 that is just large enough to faithfully describe the observed deformation at the most near-field station in our study, P496, which exhibits the most rapid changes in velocity. This ensures that σ^2 will be sufficiently large so that our estimate of $u_{\text{post}}(t)$ does not smooth out potentially valuable postseismic signal at the remaining stations. We find that using $\sigma^2 = 0.05 \text{ m}^2/\text{yr}^3$ adequately describes all but the first week of postseismic deformation at station P496, which slightly increases our estimate of coseismic displacements (Figure 2). We include an example of estimating $u_{\text{post}}(t)$ for a far-field station, P619, which is about 359 km north of the El Mayor-Cucapah epicenter (Figure 3). At station P619, along with all the other stations in the Mojave region, there is a south trending postseismic transience that persists for the first 3 years after the El Mayor-Cucapah earthquake. Postseismic deformation that extends to these epicentral distances has also been observed after the Hector Mine earthquake [Freed *et al.*, 2007].

It is important to note that the shown uncertainties in $u_{\text{post}}(t)$ do not account for the nonnegligible epistemic uncertainty in equation (2). For example, we assume a constant rate of secular deformation, which appears to be an appropriate approximation for all but perhaps the stations closest to the Hector Mine epicenter, as noted above. Also, our model for seasonal deformation in equation (2) assumes a constant amplitude over time, which means that any yearly variability in the climatic conditions could introduce systematic residuals

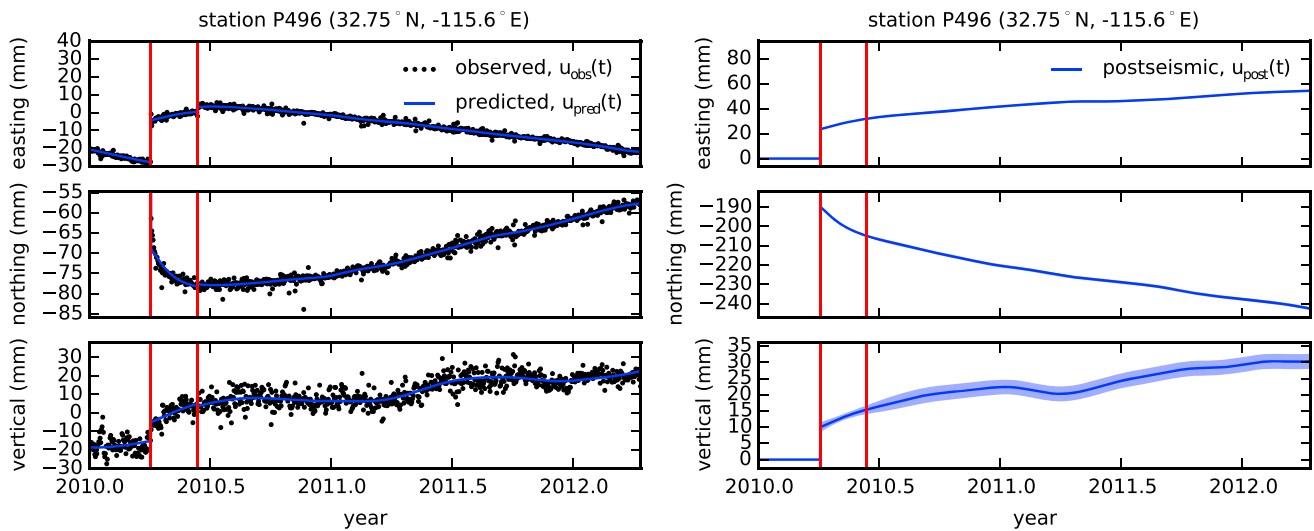


Figure 2. (left column) GPS time series from UNAVCO (black) and the predicted displacement (blue) from equation (2) for a near-field station. Red lines indicate the times of the El Mayor-Cucapah and Ocotillo earthquakes. (right column) Estimated coseismic and postseismic displacements, u_{post} , which are extracted from the predicted displacements. The 68% confidence interval is shown in light blue.

[Davis et al., 2012]. Indeed, it would be more appropriate to consider the seasonal amplitudes $c_2 - c_3$ in equation (2) as stochastic variables [Murray and Segall, 2005]. By using constant seasonal amplitudes, our estimate of $u_{post}(t)$ seems to describe some of the unmodeled annual and semiannual oscillations (e.g., Figure 3).

We show in Figures 4 and 5 the near-field and far-field coseismic displacements and the postseismic displacements accumulated over the time intervals 0–1 year, 1–3 years, and 3–5 years. Stations at epicentral distances beyond ~200 km have an elevated rate of deformation for the first 3 years following the earthquake. This far-field deformation is trending southward at a rate of a few millimeters per year along the direction of the El Mayor-Cucapah P axis. A similar eastward trend can be seen in the few far-field stations in Arizona, located along the T axis. After 3 years, the trend in far-field postseismic deformation is barely perceptible. Most far-field stations display an initial subsidence for the first year after the El Mayor-Cucapah earthquake followed by continued uplift. This trend in vertical deformation can be observed in all three of the quadrants where postseismic data are available, which means that the vertical deformation does not exhibit an antisymmetric quadrant pattern, as would be expected for postseismic processes. Although we use vertical deformation in

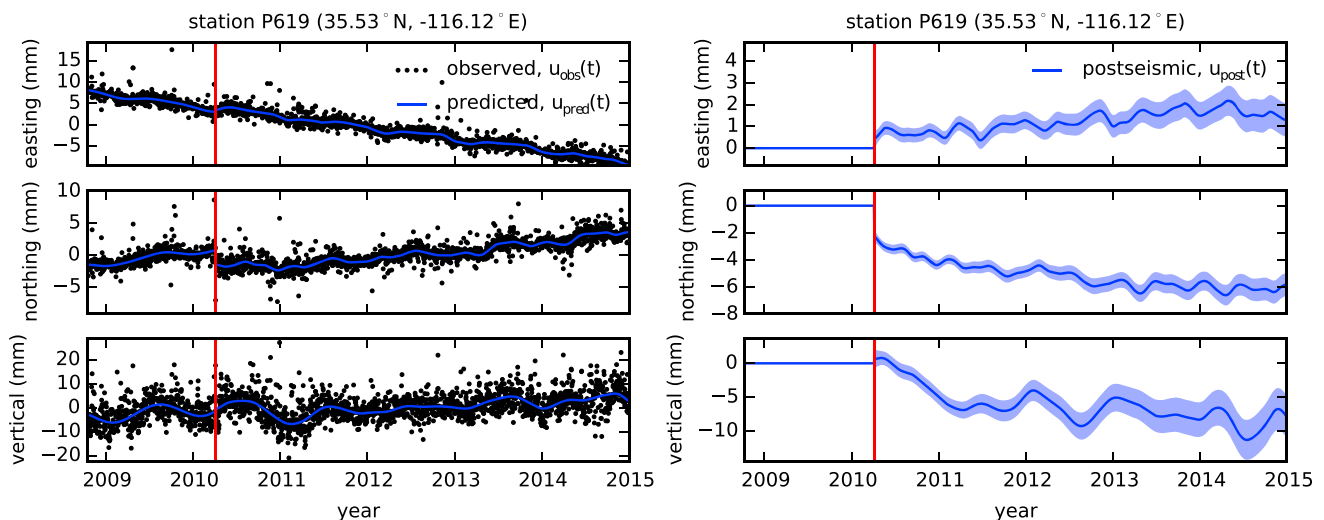


Figure 3. Same as Figure 2 but for a far-field station.

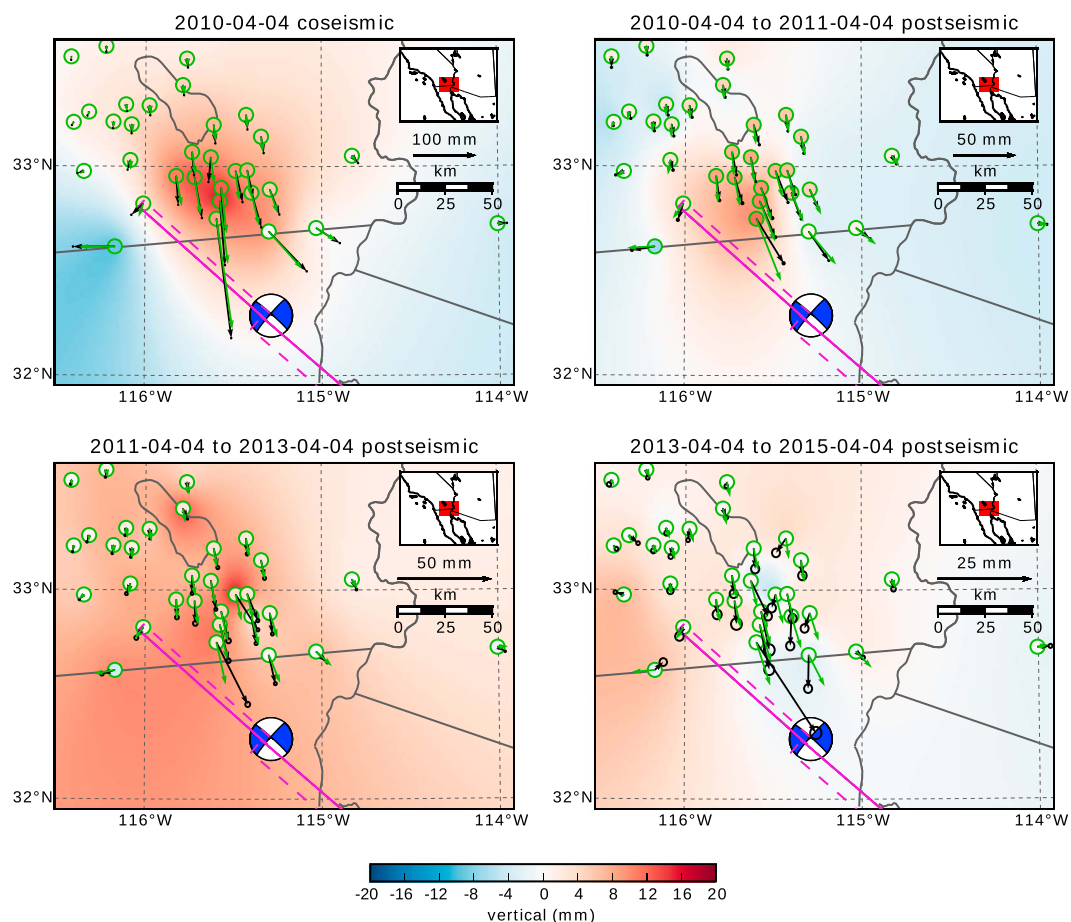


Figure 4. Near-field coseismic and cumulative postseismic displacements over the indicated time periods (black) and predicted displacements for our preferred model for section 3.3 (green). The black error ellipses show the 68% confidence interval for the observed horizontal displacements. Observed vertical displacements are shown as an interpolated field, and predicted vertical displacements are shown within the green circles. Note that the interpolant is not well constrained in Mexico where there are no data available.

our analysis in section 3, we do not put an emphasis on trying to describe the vertical deformation because it likely does not have postseismic origins.

The near-field postseismic deformation is notably sustained when compared to the far-field deformation. Namely, the station in this study which is closest to the El Mayor-Cucapah epicenter, P496, has a steady postseismic trend of ~ 1.5 cm/yr to the south after about 1 year. Vertical postseismic deformation in the near field does display a quadrant pattern which is consistent with the coseismic vertical deformation, suggesting that it is resulting from postseismic processes. However, the vertical postseismic signal is only apparent for the first year after the earthquake (Figure 4). As with the far-field deformation, there is a general trend of uplift in the near field after about 1 year.

3. Postseismic Modeling

We seek to find the mechanisms driving 5 years of postseismic deformation following the El Mayor-Cucapah earthquake, and we consider afterslip and viscoelastic relaxation as candidate mechanisms. Poroelastic rebound has also been used to model postseismic deformation [e.g., *Jónsson et al.*, 2003]; however, *Gonzalez-Ortega et al.* [2014] found that poroelastic rebound is unlikely to be a significant contributor to postseismic deformation following the El Mayor-Cucapah earthquake. Furthermore, we consider stations which are sufficiently far away from the rupture that poroelastic rebound should be insignificant.

We estimate coseismic and time-dependent postseismic fault slips, both of which are assumed to occur on a fault geometry modified from *S. Wei et al.* [2011]. Field studies [*Fletcher et al.*, 2014] and lidar observations

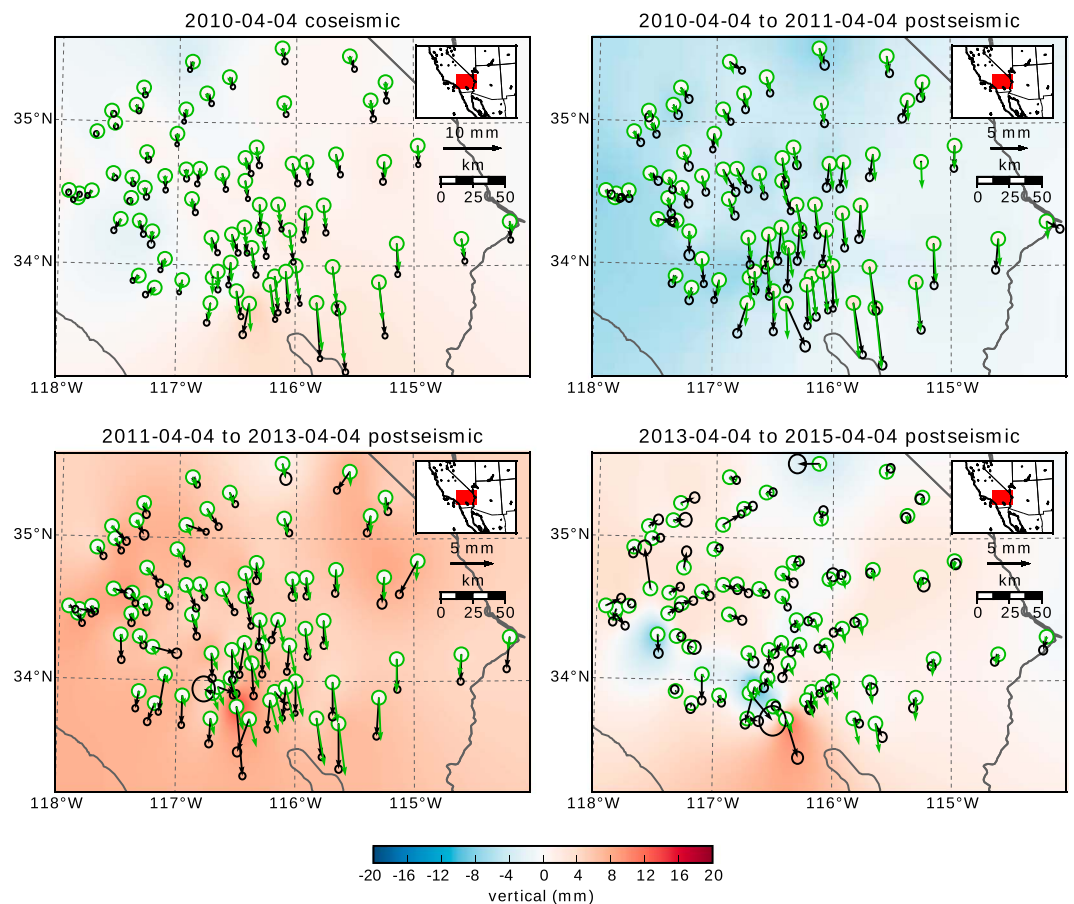


Figure 5. Same as Figure 4 but for far-field stations.

[Oskin *et al.*, 2012] have revealed a significantly more complicated fault geometry than what was inferred by *S. Wei et al.* [2011], especially within the Sierra Cucapah. However, we find that a relatively simple coseismic fault geometry based on *S. Wei et al.* [2011] is adequate because most of the stations used in this study are sufficiently far from the El Mayor-Cucapah rupture that they are insensitive to the details in the fault geometry found by *Fletcher et al.* [2014] and *Oskin et al.* [2012]. The fault geometry used in this study (Figure 1) consists of the two main fault segments inferred by *S. Wei et al.* [2011], where the northern segment runs through the Sierra Cucapah up to the U.S.-Mexico border and the southern segment is the Indiviso fault which extends down to the Gulf of California. Both segments extend from the surface to 15 km depth. We extend the northern segment by 40 km to the northwest, which is motivated by the clustering of aftershocks on the northern tip of the coseismic rupture zone [*Hauksson et al.*, 2011; *Kroll et al.*, 2013]. This extended fault segment was also found to be necessary by *Rollins et al.* [2015] and *Pollitz et al.* [2012] in order to describe the postseismic deformation.

3.1. Elastic Postseismic Inversion

We consider a variety of rheologic models for the lower crust and upper mantle. The simplest rheologic model is to consider them to be effectively elastic and isotropic. In such case, the rheologic parameters consist of the reasonably well known Lamé parameters, λ and μ , and we use the same values used by *S. Wei et al.* [2011] throughout this paper (Table 1). The only unknown is the distribution of fault slip, which can be estimated from postseismic deformation through linear least squares. *Rollins et al.* [2015] used a subset of the GPS stations considered in this study and found that 3 years of postseismic deformation following the El Mayor-Cucapah earthquake can be explained with afterslip on the coseismic fault plane without requiring any viscoelastic relaxation. We also perform an elastic slip inversion, but we use GPS stations within a larger radius about the El Mayor-Cucapah epicenter (400 km instead of ~ 200 km). Our forward problem describing predicted postseismic deformation, u_{pred} , in terms of time-dependent fault slip, s , is

$$u_{\text{pred}}(x, t) = \int_F s(\xi, t) g(x, \xi) d\xi, \quad (9)$$

Table 1. Assumed and Estimated Material Properties^a

Depth (km)	λ (GPa)	μ (GPa)	η_{eff} (10^{18} Pa s)	μ_k/μ
0–5	24.0	24.0	-	-
5–15	35.0	35.0	-	-
15–30	42.0	42.0	44.3	0.0
30–60	61.0	61.0	5.91	0.375
60–90	61.0	61.0	1.99	0.375
90–120	61.0	61.0	1.31	0.375
120–150	61.0	61.0	1.10	0.375
150– ∞	61.0	61.0	1.07	0.375

^a λ and μ are assumed known a priori and are based on the values used for the coseismic model by S. Wei *et al.* [2011]. The values for η_{eff} are estimated in section 3.2, and $\frac{\mu_k}{\mu}$ are the optimal shear moduli ratios found in section 3.3 for a Zener rheology upper mantle.

where F denotes the fault and $g(x, \xi)$ is the elastic Green's function describing displacement at surface position x resulting from slip at ξ on the fault. We estimate coseismic slip and the rate of afterslip over the postseismic time intervals 0.0–0.125, 0.125–0.25, 0.25–0.5, 0.5–1.0, 1.0–2.0, 2.0–3.0, 3.0–4.0, and 4.0–5.0 years. Each fault segment is discretized into roughly 4 km by 4 km patches, and we impose that the direction of slip and slip rate are within 45° of right lateral. We also add zeroth-order Tikhonov regularization so that our solution for s satisfies

$$\min_s \left(\left\| \frac{u_{\text{pred}}(s) - u_{\text{post}}}{\sigma_{\text{post}}} \right\|_2^2 + \lambda_s \|s\|_2^2 \right), \tag{10}$$

where σ_{post} is the uncertainty on postseismic displacements and λ_s is a penalty parameter which is chosen with a trade-off curve. We use Pylith [Aagaard *et al.*, 2013] to compute the Green's functions for this inversion as well as for the remaining inversions in this paper.

Our coseismic slip and afterslip solutions are shown in Figure 6. Similar to Rollins *et al.* [2015], we find that a large amount of afterslip on the Indiviso fault segment is required to explain the observations. The potency of our inferred coseismic slip is $3.2 \times 10^9 \text{ m}^3$, equivalent to a $M_w = 7.28$ earthquake when assuming a shear

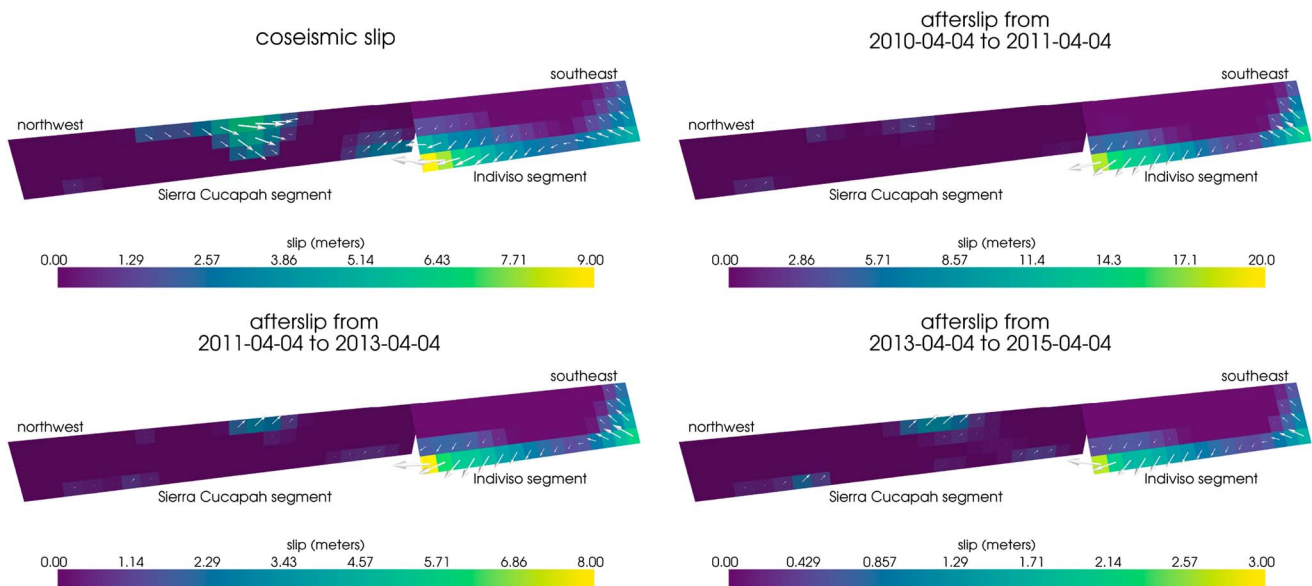


Figure 6. Coseismic slip and cumulative afterslip over the indicated time intervals when assuming that the crust and mantle are elastic. Color indicates the magnitude of slip, and arrows indicate the motion of the hanging wall.

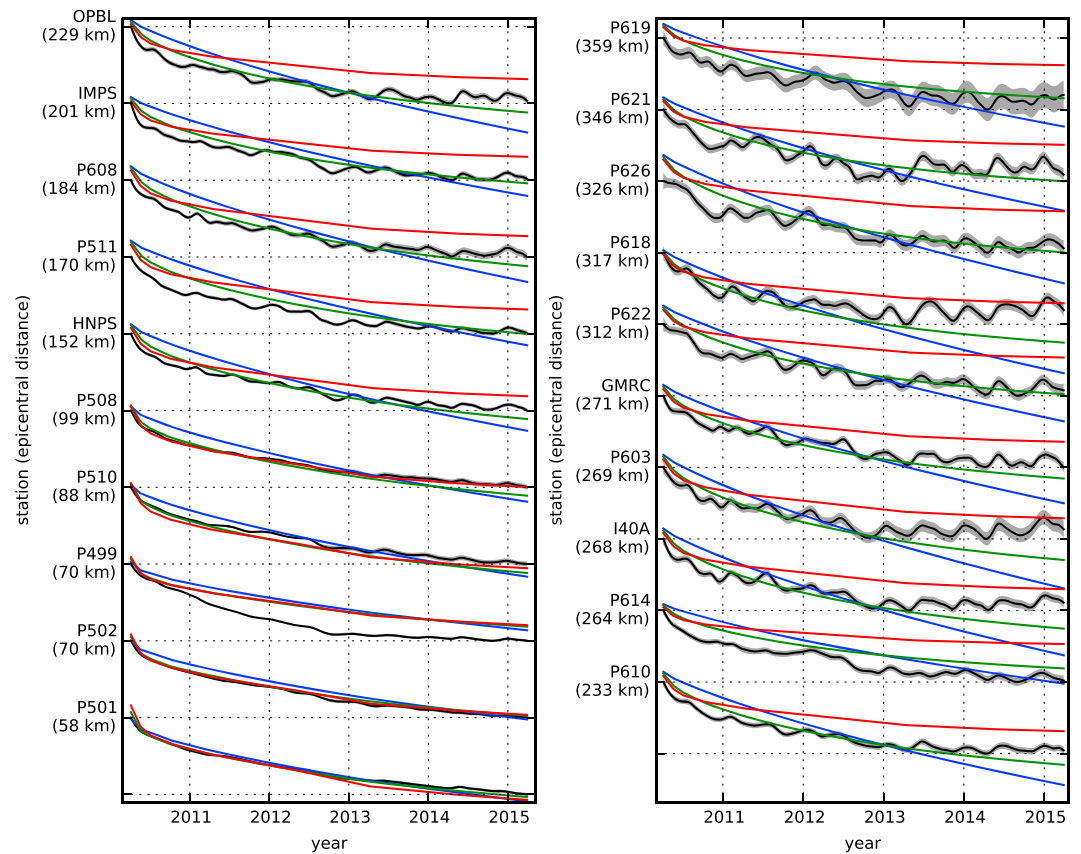


Figure 7. Scaled radial component of postseismic displacements. Downward motion indicates that the station is moving toward the El Mayor-Cucapah epicenter. Displacement time series are scaled so that the minimum and maximum observed values lie on the grid lines. The observed postseismic displacements, u_{post} , are shown in black with gray indicating the 68% confidence interval. The displacements predicted by the best fitting elastic model are shown in red. The blue and green lines are the predicted postseismic displacements for the models discussed in section 3.3. The blue lines show the predicted displacements for the model with a Maxwell viscoelastic lower crust and upper mantle. The green line shows the predicted displacements for our preferred model, which has a Maxwell viscoelastic lower crust and a Zener viscoelastic upper mantle. The effective viscosities are the same for both models and are shown in Figure 12.

modulus of 32 GPa. The potency of our inferred cumulative 5 years of afterslip is $6.1 \times 10^9 \text{ m}^3$, equivalent to a $M_w = 7.46$ earthquake, which is unrealistically large if we consider afterslip to be driven by coseismically induced stresses. Figure 7 shows the time series for the observed and predicted postseismic displacements at stations along the El Mayor-Cucapah P axis. We show the radial component of displacements with respect to the El Mayor-Cucapah epicenter, and we also rescale the displacements so that the differences between the minimum and maximum observed displacements are the same for each station. Our elastic slip model accurately describes near-field postseismic deformation and systematically underestimates postseismic deformation at epicentral distances ≥ 150 km. When the fault segments used in the inversion are extended down to 30 km depth, rather than 15 km, the systematic far-field residuals are smaller but remain apparent. Because an elastic model requires an unrealistic amount of afterslip and is unable to predict far-field deformation, we move on to consider viscoelastic models in the next section.

3.2. Early Postseismic Inversion

For any linear viscoelastic rheology of the crust and mantle, postseismic displacements resulting from time-dependent fault slip can be described as

$$u_{\text{pred}}(x, t) = \int_F s(\xi, t) g(x, \xi) d\xi + \int_0^t \int_F s(\xi, \tau) f(t - \tau, x, \xi) d\xi d\tau, \quad (11)$$

where $f(t, x, \xi)$ describes the time-dependent velocity at x resulting from viscoelastic relaxation of stresses induced by slip at ξ . f is a function of λ , μ , and any additional rheologic parameters controlling the

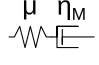
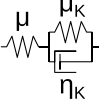
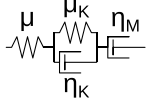
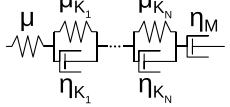
Maxwell $\eta_{\text{eff}} = \eta_M$	
Zener $\eta_{\text{eff}} = \eta_K$	
Burgers $\eta_{\text{eff}} = (1/\eta_M + 1/\eta_K)^{-1}$	
General Kelvin $\eta_{\text{eff}} = (1/\eta_M + 1/\eta_{K_1} + \dots + 1/\eta_{K_N})^{-1}$	

Figure 8. Schematic illustration of the rheologic models considered in this paper as well as their effective viscosities.

viscoelastic response, which are generally not well known. Schematic representations of the viscoelastic rheologic models considered in this study are shown in Figure 8. We discuss these rheologic models and their use in geophysical studies in section 4.

In order to greatly simplify the inverse problem, we use the method described in *Hines and Hetland* [2016] to constrain an initial effective viscosity structure from the early postseismic deformation. Our method uses the fact that coseismic stresses throughout the crust and upper mantle depend on the instantaneous elastic parameters and are independent of the viscoelastic parameters which we wish to estimate. Immediately following an earthquake, each parcel will have a strain rate that is proportional to the coseismic stress and inversely proportional to the parcel's effective viscosity, η_{eff} . Using one-dimensional rheologic models, we define the effective viscosity as

$$\eta_{\text{eff}} = \left. \frac{\sigma}{\dot{\epsilon}} \right|_{t=0}, \tag{12}$$

where σ is an applied stress at $t = 0$ and $\dot{\epsilon}$ is the resulting strain rate. Figure 8 shows how η_{eff} relates to the parameters for various linear viscoelastic rheologies. We can deduce that the initial rate of surface deformation resulting from viscoelastic relaxation is a summation of the surface deformation resulting from relaxation in each parcel, scaled by the reciprocal of the parcel's effective viscosity. That is to say

$$f(0, x, \xi) = \int_L \frac{h(x, \xi, \zeta)}{\eta_{\text{eff}}(\zeta)} d\zeta, \tag{13}$$

where L denotes the crust and mantle and $h(x, \xi, \zeta)$ describes the initial rate of deformation resulting from viscoelastic relaxation at ζ induced by slip at ξ . We can combine equation (13) with equation (11) to get a first-order approximation for early postseismic deformation,

$$u_{\text{pred}}(x, t) \approx \int_F s(\xi, t) g(x, \xi) d\xi + \int_0^t \int_F \int_L \frac{s(\tau, \xi)}{\eta_{\text{eff}}(\zeta)} h(x, \xi, \zeta) d\zeta d\xi d\tau, \tag{14}$$

which is valid for as long as the rate of deformation resulting from viscoelastic relaxation is approximately constant. Although equation (14) may only be valid for a short portion of the postseismic period, its utility becomes apparent when noting that g and h are only functions of the fault geometry and instantaneous elastic properties, λ and μ , and thus g and h can be computed numerically as a preprocessing step. The forward problem in equation (14) can then be rapidly evaluated for any realization of s and η_{eff} . This is in contrast to evaluating the full forward problem, equation (11), numerically for each realization of s and the unknown rheologic properties.

Details on how equation (14) is used to estimate s and η_{eff} from postseismic deformation can be found in *Hines and Hetland* [2016]. A nonlinear Kalman filter-based inverse method can also be used to estimate s and η_{eff} in a manner similar to *Segall and Mathews* [1997] or *McGuire and Segall* [2003], in which we would not have to explicitly impose a time-dependent parametrization of s . We have thoroughly explored Kalman filter-based

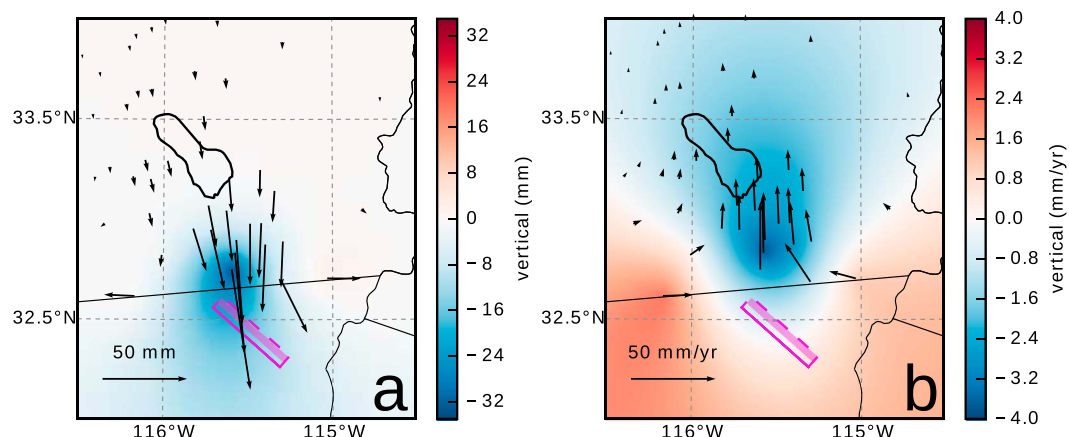


Figure 9. (a) Displacements resulting from fault slip at lower crustal depths and (b) initial velocities resulting from subsequent relaxation of a viscoelastic lower crust. The fault segment dips 75° to the northeast, and its surface projection is outlined in magenta. The highlighted area on the fault extends from 15 to 30 km depth and indicates where 1 m of right-lateral slip was imposed. The elastic properties of the crust and mantle are the same as in Table 1, and η_{eff} is 10^{18} Pa s in the lower crust. Vertical displacements are interpolated between station locations.

approaches, but we ultimately prefer the method described in *Hines and Hetland* [2016] because of its relative simplicity. Moreover, we believe that the piecewise continuous representation of slip with respect to time is sufficiently general for the resolving power of these GPS data.

We estimate coseismic slip and afterslip with the same spatial and temporal discretization as in section 3.1. Simultaneously, we estimate η_{eff} within six vertically stratified layers which have depths ranging from 15 to 30 km, 30 to 60 km, 60 to 90 km, 90 to 120 km, 120 to 150 km, and from 150 km to the bottom of our numerical model domain at 800 km. We again restrict fault slip to occur between 0 and 15 km depths, which is done in order to help eliminate inevitable nonuniqueness in the inversion. It is well understood that fault slip at sufficiently great depths can produce surface deformation that is indistinguishable from viscoelastic relaxation, at least in two-dimensional earthquake models [Savage, 1990]. Additionally, we note that when simultaneously estimating both afterslip and viscosity in the lower crust, the inverse problem becomes particularly ill posed. This ill posedness is illustrated in Figure 9, which shows the displacements resulting from a meter of slip on a fault extending from 15 to 30 km depth and the initial velocity resulting from subsequent viscoelastic relaxation in the lower crust, which is given a viscosity of 10^{18} Pa s. In this demonstration, the viscoelastic relaxation is entirely driven by the fault slip in the lower crust. The horizontal displacements from fault slip are in the opposite direction as the displacements resulting from viscoelastic relaxation. This means that surface displacements resulting from afterslip at lower crustal depths can be canceled out, at least partially, by a low-viscosity lower crust. We eliminate this null space by allowing only one mechanism in the lower crust, which we choose to be viscoelastic relaxation. This is not to say that we do not believe that deep afterslip is a possibility; rather, we restrict slip to seismogenic depths as a modeling necessity. It has been noted that the pattern of vertical postseismic deformation following the El Mayor-Cucapah earthquake indicates that a significant amount of afterslip must be shallow [Rollins et al., 2015].

We must determine at which point the early postseismic approximation breaks down, which we will denote as t_{bd} . As noted, equation (14) is valid for as long as the rate of deformation resulting from viscoelastic relaxation is approximately constant. We can almost certainly assume that deformation at the most far-field stations, which are ~ 400 km away from the El Mayor-Cucapah epicenter, is the result of viscoelastic relaxation. The approximation should then be valid for as long as a linear trend adequately approximates the far-field deformation. Using this logic, it would appear that t_{bd} is about 1 year after the El Mayor-Cucapah earthquake. Another way to determine t_{bd} is to find the best fitting prediction of equation (14) to observed deformation using increasing durations of the postseismic time series. t_{bd} should be the point when equation (14) is no longer capable of describing the observed deformation without incurring systematic misfits. When using equation (14) to fit the entire 5 years of postseismic displacements, we see that the near-field displacements (e.g., station P501) are accurately predicted. When looking at displacements in the far-field (e.g., station P621),

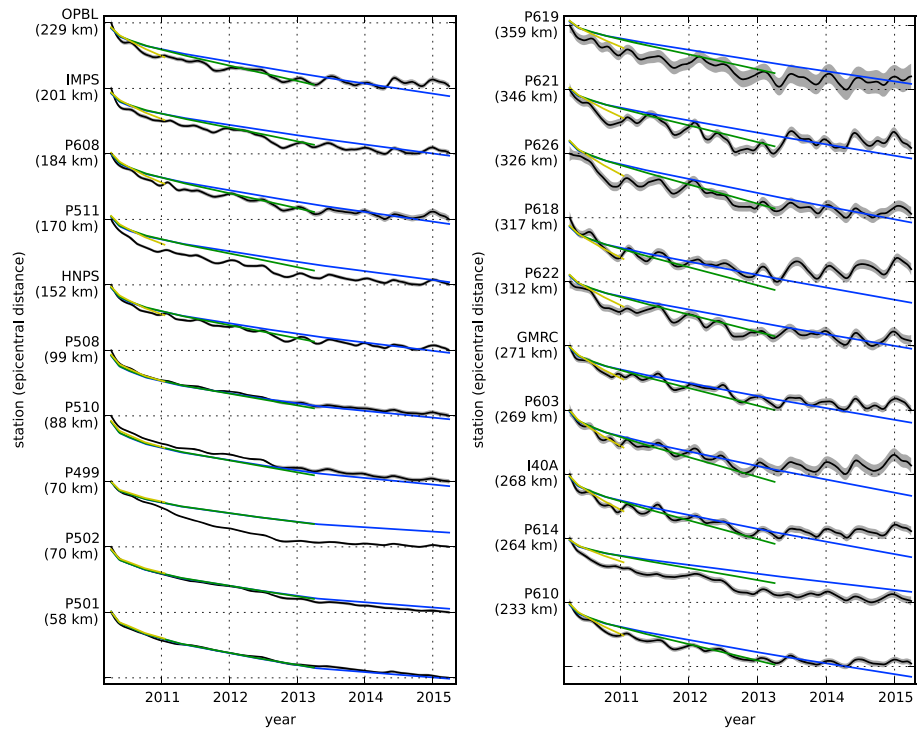


Figure 10. Observed postseismic displacements (black) and best fitting predictions of equation (14) to 5.0 (blue), 3.0 (green), and 0.8 (yellow) years of the postseismic data.

we see that equation (14) overestimates the rate of deformation in the later postseismic period and underestimates the rate of deformation in the early period (Figure 10). Due to the low signal-to-noise ratios for far-field stations, it is difficult to determine at what point equation (14) is no longer able to predict the observed displacements; however, we settle on $t_{bd} = 0.8$ year after the earthquake, while acknowledging that the choice is subjective. As noted in *Hines and Hetland [2016]*, overestimating t_{bd} will result in a bias toward overestimating η_{eff} , while picking a t_{bd} which is too low will not necessarily result in a biased estimate of η_{eff} , although the uncertainties would be larger. We can then consider inferences of η_{eff} to be an upper bound on the viscosity needed to describe the far-field rate of deformation during the first 0.8 year of postseismic deformation.

We estimate coseismic slip, afterslip, and effective viscosities by solving

$$\min_{s, \eta_{eff}} \left(\left\| \frac{u_{pred}(s, \eta_{eff}) - u_{post}}{\sigma_{post}} \right\|_2^2 + \lambda_s \|s\|_2^2 + \lambda_\eta \|\nabla \eta_{eff}^{-1}\|_2^2 \right), \quad (15)$$

where u_{post} consists of the first 0.8 year of postseismic deformation and u_{pred} are the predicted displacements from equation (14). Due to inherent nonuniqueness, we have added zeroth-order Tikhonov regularization to estimates of s and second-order Tikhonov regularization to estimates of effective fluidity, η_{eff}^{-1} . The degree to which we impose the regularization on slip and fluidity is controlled by the penalty parameters λ_s and λ_η , which are chosen with trade-off curves (Figure S1 in the supporting information). Our goal is to get a prior constraint on η_{eff} to minimize the amount of searching we have to do when describing the postseismic deformation over the full 5 years, which we do in section 3.3. Estimates of s made here will not be used in section 3.3, and so the motivation behind adding regularization to s is to ensure that the slip-driving viscoelastic relaxation in equation (14) is sensible.

Our initial estimate for coseismic slip and cumulative afterslip over the first 0.8 year after the El Mayor-Cucapah earthquake are shown in Figure 11. Similar to our elastic slip model from section 3.1, a significant amount of right-lateral and normal coseismic slip is inferred to be on the Sierra Cucapah segment. Our coseismic slip solution on the Sierra Cucapah segment is consistent with field studies [*Fletcher et al., 2014*] and the model from *S. Wei et al. [2011]*. Our inferred slip on the Indiviso fault segment differs from *S. Wei et al. [2011]* because

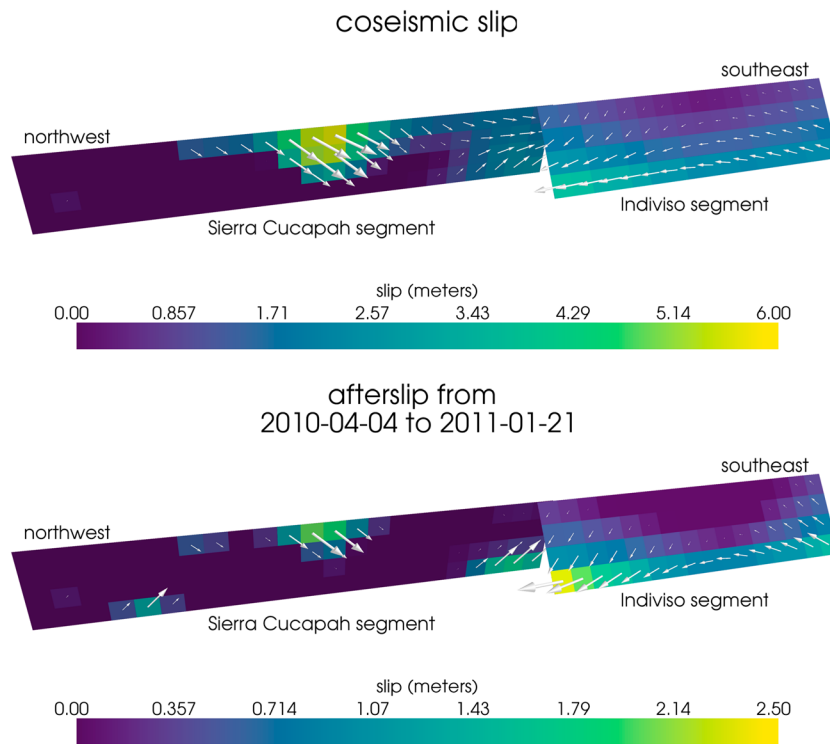


Figure 11. Coseismic slip and afterslip inferred by fitting equation (14) to the first 0.8 year of postseismic displacements.

the GPS data used in this study are not capable of resolving the spatial distribution of fault slip on that segment (Figure S2). The potency of inferred coseismic slip is $3.3 \times 10^9 \text{ m}^3$, which is also about the same as that inferred from section 3.1. The present inference of afterslip on the Indiviso fault is significantly less than what was found in section 3.1 where we did not account for viscoelasticity. When fault slip is simultaneously estimated with viscosity, the potency of inferred afterslip over the first 0.8 year after the earthquake is $0.85 \times 10^9 \text{ m}^3$, compared to $3.5 \times 10^9 \text{ m}^3$ when we assume that the crust and upper mantle are elastic. The significant amount of afterslip inferred on the Indiviso fault in section 3.1 seems to be compensating for unmodeled viscoelastic relaxation. The fact that there is still an appreciable amount of afterslip inferred on the Indiviso fault raises the question of whether it is compensating for viscoelastic relaxation that is more localized than what we allow for since we only estimate depth-dependent variations in viscosity.

Our estimated effective viscosities, and corresponding fluidities, are shown in Figure 12. Although fluidity is rarely used in geophysical literature, equation (13) is linear with respect to fluidity and so the fluidity indicates the amplitude of the viscoelastic signal coming from each layer. We use bootstrapping to find the 95% confidence intervals for our estimated effective viscosities which are shown as shaded regions in Figure 12. It is important to remember that the presented effective viscosities were estimated with a smoothing regularization constraint, and so the uncertainties are almost certainly underestimated [Aster *et al.*, 2011]. Indeed, many viscosity profiles which are outside of the shown confidence intervals can just as adequately describe the first 0.8 year of postseismic deformation. Our solution in Figure 12 should be interpreted as the smoothest effective viscosity profile which is capable of describing the data. This means that any sharp viscosity transitions will be tapered out in the inversion, which we demonstrate with a synthetic test in Figure S2. Nonetheless, a robust feature that we see with a variety of choices for λ_s , λ_{η} , and t_{bd} is that the largest jump in fluidity is at 60 km depth, which is consistent with the range of lithosphere-asthenosphere boundary depths inferred by Lekic *et al.* [2011]. This transitional depth is also consistent with the viscosity structure required to explain far-field postseismic deformation following the Hector Mine earthquake [Freed *et al.*, 2007]. We find that the viscosity below 60 km depth needs to be $\sim 1 \times 10^{18} \text{ Pa s}$ to describe the early rate of postseismic deformation at far-field stations while the lower crust and uppermost mantle need to be relatively stronger. The viscosity of the lower crust has the largest uncertainty because there is no evidence of relaxation in that layer,

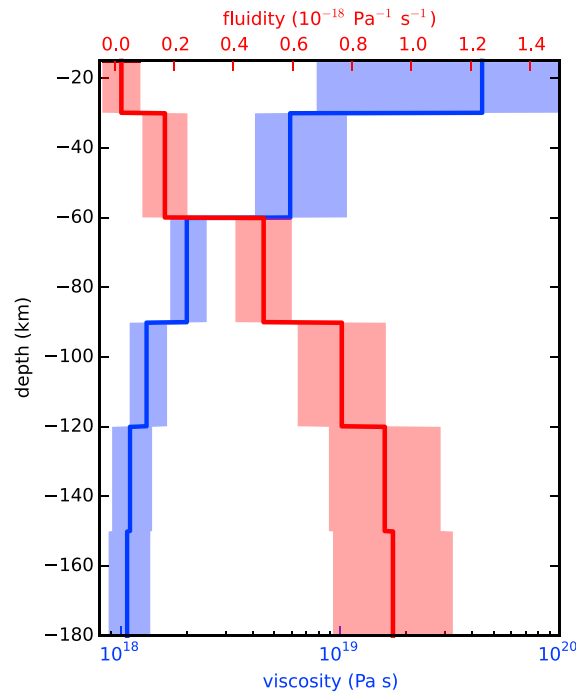


Figure 12. Effective viscosities and associated fluidities inferred by fitting equation (14) to the first 0.8 year of postseismic displacements. The 95% confidence intervals, estimated from bootstrapping, are indicated by shaded regions.

ence of η_{eff} . We compute f and g from equation (11) using Pylith, and we use the same spatial and temporal discretization of s as in sections 3.1 and 3.2. We estimate s using linear least squares and find a misfit of $\bar{\chi}^2 = 37.4$. For comparison, $\bar{\chi}^2 = 35.3$ for the elastic model from section 3.1. The Maxwell viscoelastic model has a larger misfit because it tends to overestimate the rate of deformation after about 3 years (Figure 7). Since our initial estimates of η_{eff} may be biased toward overestimating viscosities, we have also performed the slip inversion where we use uniformly lower viscosities in the crust and mantle; however, decreasing the viscosity only increases the misfit. Although, the viscosities used here are consistent with the successful Maxwell viscoelastic models found by *Rollins et al.* [2015] and *Spinler et al.* [2015], which had mantle viscosities on the order of 10^{18} Pa s and relatively higher lower crustal viscosities, we find that such a model is incapable of describing the entire postseismic time series. *Pollitz et al.* [2001] similarly recognized this deficiency in a Maxwell rheology, which then motivated their exploration of a Burgers rheology upper mantle [*Pollitz*, 2003].

Instead of exploring a Burgers rheology mantle, which introduces two new parameters that need to be estimated, the transient viscosity, η_K , and transient shear modulus, μ_K , we first consider a Zener rheology for the mantle, which only introduces one unknown model parameter, μ_K . We assume that the lower crust still has a Maxwell rheology. The steady-state viscosity in the crust and the transient viscosity in the mantle are set equal to the inferred effective viscosities. We then estimate the ratio of shear moduli, $\frac{\mu_K}{\mu}$. We compute nine different sets of Green's functions, f and g , where we assume values of $\frac{\mu_K}{\mu}$ ranging from 0 to 1. The former being a degenerate case where the Zener model reduces to the above Maxwell model. We estimate coseismic slip and afterslip for each realization of $\frac{\mu_K}{\mu}$. We find that a shear moduli ratio of 0.375 yields the best prediction to the observed postseismic displacements with a misfit of $\bar{\chi}^2 = 31.2$ (Figure 13). The improvement in the Zener model over the Maxwell model can be seen in the fit to the far-field data (Figure 7) where the Zener model does a significantly better job at explaining the transient rate of deformation throughout the 5 years considered in this study. The rheologic parameters for our preferred Zener model are summarized in Table 1.

Because we are able to adequately describe the available 5 years of postseismic deformation with a Zener model, we do not find it necessary to explore the parameter space for a more complicated Burgers rheology. However, since the Zener model is a Burgers model with an infinite steady-state viscosity, we can conclude that any Burgers rheology that has a transient viscosity consistent with that found in section 3.2 and a steady-state

meaning that it is effectively elastic over the first 0.8 year after the earthquake.

3.3. Full Postseismic Inversion

In the previous section, we used the inverse method from *Hines and Hetland* [2016] to constrain the effective viscosity structure required to explain the first 0.8 year of postseismic deformation. In this section, we use these effective viscosities as a prior constraint when searching for models which are capable of describing the available 5 years of postseismic data, where our forward problem is now equation (11) rather than the approximation given by equation (14). We perform a series of fault slip inversions assuming a variety of rheologies for the lower crust and upper mantle which are consistent with our findings from section 3.2. We appraise each model using the mean chi-square value,

$$\bar{\chi}^2 = \frac{1}{N} \left\| \frac{u_{\text{pred}} - u_{\text{post}}}{\sigma_{\text{post}}} \right\|_2^2, \quad (16)$$

where N is the number of observations.

We first assume that the crust and mantle can be described with a Maxwell rheology, and we set the steady-state viscosity, η_M , equal to our infer-

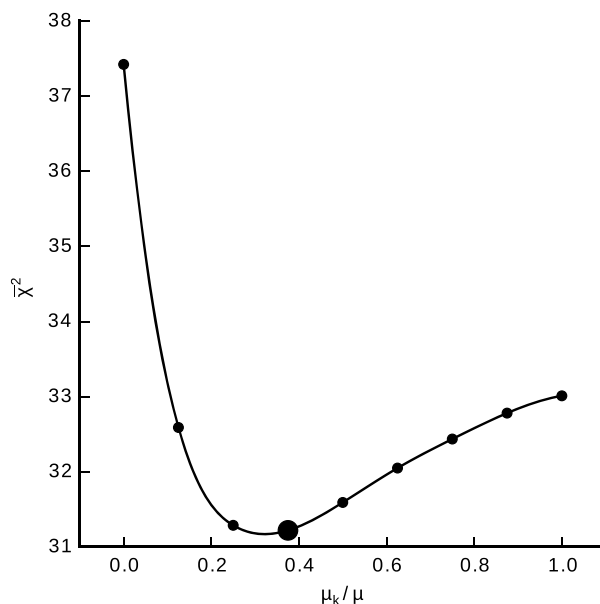


Figure 13. Mean chi-square value as a function of the transient shear modulus relative to the elastic shear modulus in a Zener rheology upper mantle. Large dot indicates our preferred ratio.

viscosity $\gtrsim 10^{20}$ Pa s, which is effectively infinite on the timescale of 5 years, would also be able to satisfactorily describe the observable postseismic deformation.

The regularized inference of coseismic slip and afterslip for our preferred Zener model is shown in Figure 14. The inferred coseismic potency is 3.0×10^9 m³, equivalent to a $M_w = 7.26$ earthquake, where most of the slip is shallow and on the Sierra Cucapah fault segment. The potency of 5 years of afterslip is 1.1×10^9 m³. Most of the afterslip in our preferred model occurs within the first year after the earthquake and coincides with the location of our inferred coseismic slip. Inferred afterslip within the first year is accounting for the most rapid near-field transient deformation (Figure S3). After 1 year, afterslip is inferred to be deeper down on the Sierra Cucapah segment. The sustained near-field postseismic deformation is being explained by this continued afterslip as well as viscoelastic

relaxation in the lower crust. We emphasize that the GPS station closest to where we infer afterslip, P496, is still about 30 km away, which is too far for us to conclusively discern deep afterslip from viscoelastic relaxation in the lower crust. The deep afterslip inferred after 1 year could potentially be compensating for an overestimated lower crustal viscosity. To test this, we have modified our preferred model by decreasing the lower crustal viscosity from 5.91×10^{19} Pa s to 1×10^{19} Pa s, which is still consistent with our viscosity inference from section 3.2, and we inverted for fault slip. We find that a model with a weaker lower crust adequately describes the postseismic displacements without any afterslip after 1 year, while still requiring about the same amount of afterslip over the first year. We do believe that the early afterslip on the Sierra Cucapah segment is a robust feature in our preferred model, while we are not confident in our inference of later deep afterslip.

The postseismic displacements predicted by our preferred Zener model are shown in Figures 4, 5, and 7. The largest misfit occurs within the Imperial Valley where there does not appear to be any systematic trend in the

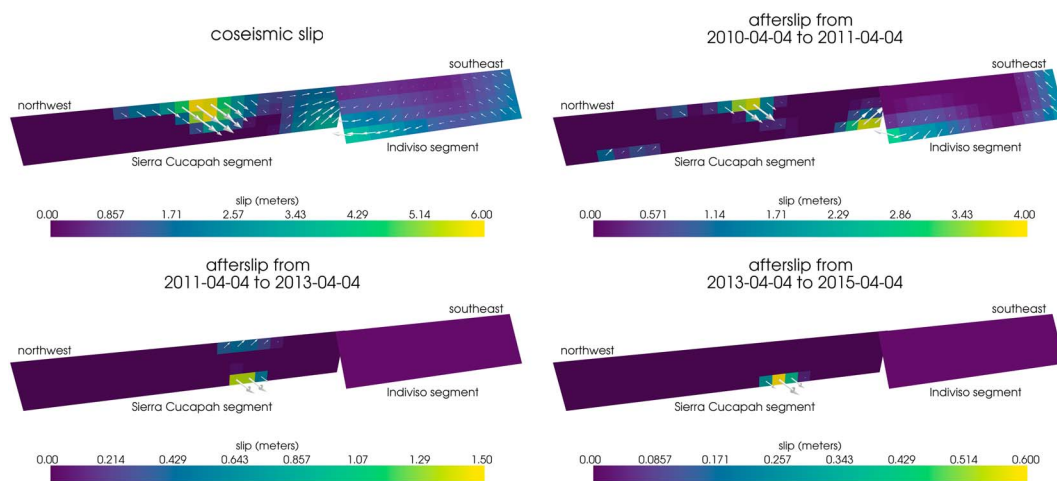


Figure 14. Inferred coseismic slip and afterslip for our preferred model, which has a Maxwell rheology in the lower crust and a Zener rheology in the upper mantle. The transient viscosity, η_K , in the mantle and steady-state viscosity, η_M , in the crust are set equal to the effective viscosities from Figure 12. We use $\frac{\mu_K}{\mu} = 0.375$ in the upper mantle.

residuals. This suggests that the large errors are due to localized processes such as fault slip in the Imperial Valley triggered by the El Mayor-Cucapah earthquake [M. Wei *et al.*, 2011, 2015]. We do not see any pattern in the residuals that would suggest a laterally heterogeneous viscosity structure, which has been explored by Pollitz *et al.* [2012] and Rollins *et al.* [2015]. We do notice regional-scale seasonal oscillations in the lateral and vertical components of the residuals with an amplitude of 1–2 mm. This is the result of our method for data processing which is not able to completely remove the seasonal signal in the GPS data, which was discussed in section 2. Additionally, we see systematic misfit in the later postseismic period west of the Landers and Hector Mine earthquakes, which may be the result of unmodeled postseismic deformation following those earthquakes. Lastly, there are clear discrepancies between the observed and predicted vertical displacements following the first year after the El Mayor-Cucapah earthquake. We observe a broad uplift throughout Southern California which is inconsistent with any postseismic model.

4. Discussion

It has long been recognized that deep afterslip and viscoelastic relaxation following an upper crustal earthquake can result in similar horizontal ground deformation at the surface [e.g., Savage, 1990; Pollitz *et al.*, 2001; Hearn, 2003; Feigl and Thatcher, 2006]. The similarity of the horizontal postseismic deformation results in a nonuniqueness in inferences of afterslip or viscoelastic relaxation. The spatial pattern of vertical postseismic deformation has been proposed to be a discriminant between deep afterslip and viscoelastic relaxation [e.g., Pollitz *et al.*, 2001; Hearn, 2003]. It is, however, important to note that patterns of vertical deformation are very sensitive to the depth dependence of viscosity below the upper crust [Yang and Toksöz, 1981; Hetland and Zhang, 2014]. The similarity between deformation resulting from deep afterslip and viscoelastic relaxation of coseismic stresses is different from the ill posedness described in section 3.2. In our method, any inferred afterslip will also mechanically drive additional viscoelastic relaxation. The horizontal deformation resulting from deep afterslip will generally be in the opposite direction as horizontal deformation resulting from viscoelastic relaxation of subsequent stresses in the lower crust (Figure 9). As a result, there is a trade-off between inferences of deep afterslip and lower crustal viscosity. In our synthetic tests in Hines and Hetland [2016], we have found that inverting surface deformation for afterslip and viscosity within the same depth interval tends to result in overestimated afterslip and an underestimated viscosity.

Most postseismic studies assume Maxwell viscoelasticity in the lower crust and upper mantle [e.g., Nur and Mavko, 1974; Pollitz *et al.*, 2000; Hetland, 2003; Freed *et al.*, 2006; Johnson *et al.*, 2009; Hearn *et al.*, 2009], which is the simplest viscoelastic rheologic model. In Southern California, postseismic studies following the Landers [Pollitz *et al.*, 2000], Hector Mine [Pollitz *et al.*, 2001], and El Mayor-Cucapah earthquake [Spinler *et al.*, 2015; Rollins *et al.*, 2015] have assumed Maxwell viscoelasticity in the lower crust and upper mantle and have inferred upper mantle viscosities on the order of 10^{17} to 10^{18} Pa s and lower crust viscosities $\gtrsim 10^{19}$ Pa s. These postseismic studies are consistent with Kaufmann and Amelung [2000] and Cavalié *et al.* [2007], who found that an upper mantle viscosity of 10^{18} Pa s and a crustal viscosity $\gtrsim 10^{20}$ Pa s are necessary to describe subsidence resulting from changes in loading from Lake Mead. This isostatic adjustment is a process with similar spatial and temporal scales as postseismic deformation, and thus the inferred viscosities of these two types of studies would likely agree. While these studies found viscosities that are consistent with our effective viscosities from section 3.2, they are inconsistent with viscosity estimates made from geophysical processes that occur over longer timescales. For example, Lundgren *et al.* [2009] found that lower crust and upper mantle viscosities on the order of 10^{21} and 10^{19} Pa s, respectively, are needed to describe interseismic deformation along the Southern San Andreas Fault zone in the Salton Sea region. An even higher mantle viscosity, on the order of 10^{20} Pa s, is required to describe isostatic adjustment resulting from the draining of Lake Bonneville, which occurs on the timescales of 10^4 years [Crittenden, 1967; Bills and May, 1987].

An additional deficiency with the Maxwell rheology is that it predicts a steady decay in the rate of postseismic deformation over time, which fails to describe the commonly observed rapid, early transience followed by a relatively steady rate of postseismic deformation. One could explain the early transient postseismic deformation with fault creep and the later phase with relaxation in a Maxwell viscoelastic lower crust and upper mantle [e.g., Hearn *et al.*, 2009; Johnson *et al.*, 2009]. However, postseismic deformation at distances greater than ~ 200 km from the El Mayor-Cucapah epicenter can only be attributed to viscoelastic relaxation [e.g., Freed *et al.*, 2007] and we have demonstrated that the far-field deformation cannot be explained with a Maxwell rheology (Figure 7).

We found that a Zener rheology in the upper mantle with a transient viscosity of $\sim 10^{18}$ Pa s does a noticeably better job at predicting far-field postseismic deformation. A generalization of the Zener viscoelastic model, schematically represented as several Kelvin elements connected in series, is commonly used to describe seismic attenuation [Liu *et al.*, 1976]. The highest viscosity needed to describe seismic attenuation is on the order of 10^{16} Pa s [Yuen and Peltier, 1982] which has a characteristic relaxation time on the order of days. Even though our inferred transient viscosity is orders of magnitude larger than that required for seismic attenuation models, the two models are not incompatible. Rather, the delayed elasticity in seismic attenuation models occurs on such short timescales that it can be considered part of the instantaneous elastic phase of deformation associated with the preferred Zener model in this study.

Of course, a Zener rheology provides an incomplete description of the asthenosphere because it does not have the fluid-like behavior required to explain isostatic rebound or convection in the mantle [O'Connell, 1971]. Yuen and Peltier [1982] proposed a Burgers rheology with a low transient viscosity ($\eta_K \approx 10^{16}$ Pa s) and high steady-state viscosity ($\eta_M \approx 10^{21}$ Pa s) to describe both seismic attenuation and long-term geologic processes. The justification of a Burger's rheology mantle is further supported by laboratory experiments on olivine [Chopra, 1997]. Pollitz [2003] sought to describe postseismic deformation following Hector Mine with a Burgers rheology mantle, and they found a best fitting transient viscosity of 1.6×10^{17} Pa s and steady-state viscosity of 4.6×10^{18} Pa s. While the Burgers rheology was introduced as a means of bridging the gap between relaxation observed in long- and short-term geophysical processes, the inferred steady-state viscosity from Pollitz [2003] is still inconsistent with the Maxwell viscosities inferred from studies on the earthquake cycle and Lake Bonneville. The transient viscosity inferred by Pollitz [2003] is constrained by the earliest phase of postseismic deformation following the Hector Mine earthquake. While Pollitz [2003] ruled out deep afterslip as an alternative mechanism based on inconsistent vertical deformation, it is still possible to successfully describe all components of early postseismic deformation following the Hector Mine earthquake with afterslip at seismogenic depths [Jacobs *et al.*, 2002]. It is then possible that the preferred rheologic model from Pollitz [2003] was biased toward inferring a particularly low transient viscosity by neglecting to account for afterslip. This is in contrast to the present study, where we have inferred a viscosity structure simultaneously with afterslip. We also argue that a transient rheology is necessary to explain postseismic deformation; however, our preferred transient viscosity of $\sim 10^{18}$ Pa s in the upper mantle is an order of magnitude larger than the transient viscosity found by Pollitz [2003]. The transient viscosity inferred here is consistent with the results of Pollitz [2015], who reanalyzed postseismic data following the Landers and Hector Mine earthquake allowing the first few months of transient deformation to be described by afterslip. Since a Zener model is able to describe the available postseismic deformation following the El Mayor-Cucapah earthquake, any Burgers rheology with a steady-state viscosity that is $\geq 10^{20}$ Pa s, effectively infinite over 5 years, would also be able to describe the postseismic deformation. Such a Burgers model might then be consistent with the steady-state viscosities necessary for lake loading, interseismic deformation, and mantle dynamics.

5. Conclusion

We have extracted a smoothed estimate of postseismic deformation following the El Mayor-Cucapah earthquake from GPS displacement time series. Our estimated postseismic deformation reveals far-field (epicentral distances ≥ 200 km) transient deformation which is undetectable after about 3 years. Near-field deformation exhibits transience that decays to a sustained, elevated rate after about 1 or 2 years. We found that near-field transient deformation can be explained with shallow afterslip. The sustained rate of near-field deformation can be explained with viscoelastic relaxation in the lower crust and possibly continued afterslip. Far-field transient deformation can be more definitively ascribed to viscoelastic relaxation at depths greater than ~ 60 km. Beneath that depth, a transient viscosity of $\sim 1 \times 10^{18}$ Pa s is required to describe the rate of far-field deformation throughout the 5 years considered in this study. By describing the available postseismic deformation with a transient rheology in the mantle, our preferred model does not conflict with the generally higher steady-state viscosities inferred from geophysical processes occurring over longer timescales.

References

- Aagaard, B. T., M. G. Knepley, and C. A. Williams (2013), A domain decomposition approach to implementing fault slip in finite-element models of quasi-static and dynamic crustal deformation, *J. Geophys. Res. Solid Earth*, 118, 3059–3079, doi:10.1002/jgrb.50217.
- Argus, D. F., M. B. Heflin, G. Peltzer, F. Crampé, and F. H. Webb (2005), Interseismic strain accumulation and anthropogenic motion in metropolitan Los Angeles, *J. Geophys. Res.*, 110, B04401, doi:10.1029/2003JB002934.
- Aster, R. C., B. Borchers, and C. H. Thurber (2011), *Parameter Estimation and Inverse Problems*, vol. 90, Academic Press, Burlington, Mass.

Acknowledgments

We thank Andy Freed for an illuminating discussion on the data used in this study. We thank Fred Pollitz and an anonymous reviewer for their comments that improved this manuscript. This material is based on EarthScope Plate Boundary Observatory data services provided by UNAVCO through the GAGE Facility with support from the National Science Foundation (NSF) and National Aeronautics and Space Administration (NASA) under NSF Cooperative Agreement EAR-1261833. The data used in this study can be found at www.unavco.org. This material is based upon work supported by the National Science Foundation under grants EAR 1045372 and EAR 1245263.

- Bawden, G. W., W. Thatcher, R. S. Stein, K. W. Hudnut, and G. Peltzer (2001), Tectonic contraction across Los Angeles after removal of groundwater pumping effects, *Nature*, *412*, 812–815, doi:10.1038/35090558.
- Bills, B. G., and G. M. May (1987), Lake Bonneville: Constraints on lithospheric thickness and upper mantle viscosity from isostatic warping of Bonneville, Provo, and Gilbert Stage Shorelines, *J. Geophys. Res.*, *92*(B11), 11,493–11,508, doi:10.1029/JB092iB11p11493.
- Çakir, Z., S. Ergintav, H. Özener, U. Dogan, A. M. Akoglu, M. Meghraoui, and R. Reilinger (2012), Onset of aseismic creep on major strike-slip faults, *Geology*, *40*(12), 1115–1118, doi:10.1130/G33522.1.
- Cavalié, O., M. P. Doin, C. Lasserre, and P. Briole (2007), Ground motion measurement in the Lake Mead area, Nevada, by differential synthetic aperture radar interferometry time series analysis: Probing the lithosphere rheological structure, *J. Geophys. Res.*, *112*, B03403, doi:10.1029/2006JB004344.
- Cetin, E., Z. Cakir, M. Meghraoui, S. Ergintav, and A. M. Akoglu (2014), Extent and distribution of aseismic slip on the Ismetpasa segment of the North Anatolian Fault (Turkey) from Persistent Scatterer InSAR, *Geochem. Geophys. Geosyst.*, *15*, 2883–2894, doi:10.1002/2014GC005307.
- Chopra, P. N. (1997), High-temperature transient creep in olivine rocks, *Tectonophysics*, *279*, 93–111, doi:10.1016/S0040-1951(97)00134-0.
- Crittenden, M. (1967), Viscosity and finite strength of the mantle as determined from water and ice loads, *Geophys. J. R. Astron. Soc.*, *14*, 261–279, doi:10.1111/j.1365-246X.1967.tb06243.x.
- Davis, J. L., B. P. Wernicke, and M. E. Tamisiea (2012), On seasonal signals in geodetic time series, *J. Geophys. Res.*, *117*, B01403, doi:10.1029/2011JB008690.
- Feigl, K. L., and W. Thatcher (2006), Geodetic observations of post-seismic transients in the context of the earthquake deformation cycle, *C. R. Geosci.*, *338*, 1012–1028, doi:10.1016/j.crte.2006.06.006.
- Fletcher, J. M., et al. (2014), Assembly of a large earthquake from a complex fault system: Surface rupture kinematics of the 4 April 2010 El Mayor-Cucapah (Mexico) M_w 7.2 earthquake, *Geosphere*, *10*(4), 797–827, doi:10.1130/GES00933.1.
- Freed, A. M., R. Bürgmann, E. Calais, J. Freymueller, and S. Hreinsdóttir (2006), Implications of deformation following the 2002 Denali, Alaska, earthquake for postseismic relaxation processes and lithospheric rheology, *J. Geophys. Res.*, *111*, B01401, doi:10.1029/2005JB003894.
- Freed, A. M., R. Bürgmann, and T. Herring (2007), Far-reaching transient motions after Mojave earthquakes require broad mantle flow beneath a strong crust, *Geophys. Res. Lett.*, *34*, L19302, doi:10.1029/2007GL030959.
- Gonzalez-Ortega, A., Y. Fialko, D. Sandwell, F. A. Nava-pichardo, J. Fletcher, J. Gonzalez-garcia, B. Lipovsky, M. Floyd, and G. Funning (2014), El Mayor-Cucapah (M_w 7.2) earthquake: Early near-field postseismic deformation from InSar and GPS observations, *J. Geophys. Res. Solid Earth*, *119*, 1482–1497, doi:10.1002/2013JB010193.
- Hauksson, E., J. Stock, K. Hutton, W. Yang, J. A. Vidal-Villegas, and H. Kanamori (2011), The 2010 M_w 7.2 El Mayor-Cucapah earthquake sequence, Baja California, Mexico and Southernmost California, USA: Active seismotectonics along the Mexican Pacific margin, *Pure Appl. Geophys.*, *168*, 1255–1277, doi:10.1007/s00024-010-0209-7.
- Hearn, E. H. (2003), What can GPS data tell us about the dynamics of post-seismic deformation, *Geophys. J. Int.*, *115*, 753–777, doi:10.1111/j.1365-246X.2003.02030.x.
- Hearn, E. H., S. McClusky, S. Ergintav, and R. E. Reilinger (2009), Izmit earthquake postseismic deformation and dynamics of the North Anatolian Fault Zone, *J. Geophys. Res.*, *114*, B08405, doi:10.1029/2008JB006026.
- Hetland, E. A. (2003), Postseismic relaxation across the Central Nevada Seismic Belt, *J. Geophys. Res.*, *108*(B8), 2394, doi:10.1029/2002JB002257.
- Hetland, E. A., and G. Zhang (2014), Effect of shear zones on post-seismic deformation with application to the 1997 M_w 7.6 Manyi earthquake, *Geophys. J. Int.*, *206*(2), 1–11, doi:10.1093/gji/ggu127.
- Hines, T. T., and E. A. Hetland (2013), Bias in estimates of lithosphere viscosity from interseismic deformation, *Geophys. Res. Lett.*, *40*, 4260–4265, doi:10.1002/grl.50839.
- Hines, T. T., and E. A. Hetland (2016), Rapid and simultaneous estimation of fault slip and heterogeneous lithospheric viscosity from post-seismic deformation, *Geophys. J. Int.*, *204*(1), 569–582, doi:10.1093/gji/ggv477.
- Jacobs, A., D. Sandwell, Y. Fialko, and L. Sichoix (2002), The 1999 (M_w 7.1) Hector Mine, California, earthquake: Near-field postseismic deformation from ERS interferometry, *Bull. Seismol. Soc. Am.*, *92*(4), 1433–1442.
- Johnson, K. M., and P. Segall (2004), Viscoelastic earthquake cycle models with deep stress-driven creep along the San Andreas fault system, *J. Geophys. Res.*, *109*, B10403, doi:10.1029/2004JB003096.
- Johnson, K. M., R. Bürgmann, and J. T. Freymueller (2009), Coupled afterslip and viscoelastic flow following the 2002 Denali Fault, Alaska earthquake, *Geophys. J. Int.*, *176*(3), 670–682, doi:10.1111/j.1365-246X.2008.04029.x.
- Jónsson, S., P. Segall, R. Pedersen, and G. Björnsson (2003), Post-earthquake ground movements correlated to pore-pressure transients, *Nature*, *424*, 179–183, doi:10.1038/nature01758.1.
- Kaufmann, G., and F. Amelung (2000), Reservoir-induced deformation and continental rheology in vicinity of Lake Mead, Nevada, *J. Geophys. Res.*, *105*(B7), 16,341–16,358, doi:10.1029/2000JB900079.
- Kroll, K. A., E. S. Cochran, K. B. Richards-Dinger, and D. F. Sumy (2013), Aftershocks of the 2010 M_w 7.2 El Mayor-Cucapah earthquake reveal complex faulting in the Yuha Desert, California, *J. Geophys. Res. Solid Earth*, *118*, 6146–6164, doi:10.1002/2013JB010529.
- Lekic, V., S. W. French, and K. M. Fischer (2011), Lithospheric thinning beneath rifted regions of Southern California, *Science*, *334*, 783–787.
- Liu, H.-P., D. L. Anderson, and H. Kanamori (1976), Velocity dispersion due to anelasticity: Implications for seismology and mantle composition, *Geophys. J. R. Astron. Soc.*, *47*, 41–58, doi:10.1111/j.1365-246X.1976.tb01261.x.
- Lundgren, P., E. A. Hetland, Z. Liu, and E. J. Fielding (2009), Southern San Andreas-San Jacinto fault system slip rates estimated from earthquake cycle models constrained by GPS and interferometric synthetic aperture radar observations, *J. Geophys. Res.*, *114*, B02403, doi:10.1029/2008JB005996.
- McGuire, J. J., and P. Segall (2003), Imaging of aseismic fault slip transients recorded by dense geodetic networks, *Geophys. J. Int.*, *155*, 778–788, doi:10.1111/j.1365-246X.2003.02022.x.
- Meade, B. J., and B. H. Hager (2005), Block models of crustal motion in southern California constrained by GPS measurements, *J. Geophys. Res.*, *110*, B03403, doi:10.1029/2004JB003209.
- Murray, J. R., and P. Segall (2005), Spatiotemporal evolution of a transient slip event on the San Andreas fault near Parkfield, California, *J. Geophys. Res.*, *110*, B09407, doi:10.1029/2005JB003651.
- Nur, A., and G. Mavko (1974), Postseismic viscoelastic rebound, *Science*, *183*(4121), 204–206, doi:10.1038/098448b0.
- O'Connell, R. J. (1971), Rheology of the mantle, *Eos Trans. AGU*, *52*, 140–142.
- Oskin, M. E., et al. (2012), Near-field deformation from the El Mayor-Cucapah earthquake revealed by differential LIDAR, *Science*, *335*, 702–705, doi:10.1126/science.1213778.
- Pollitz, F., C. Wicks, and W. Thatcher (2001), Mantle flow beneath a continental strike-slip fault: Postseismic deformation after the 1999 Hector Mine earthquake, *Science*, *293*, 1814–1818, doi:10.1126/science.1061361.

- Pollitz, F. F. (2003), Transient rheology of the uppermost mantle beneath the Mojave Desert, California, *Earth Planet. Sci. Lett.*, *215*, 89–104, doi:10.1016/S0012-821X(03)00432-1.
- Pollitz, F. F. (2015), Postearthquake relaxation evidence for laterally variable viscoelastic structure and water content in the Southern California mantle, *J. Geophys. Res. Solid Earth*, *120*, 2672–2696, doi:10.1002/2014JB011603.
- Pollitz, F. F., G. Peltzer, and R. Bürgmann (2000), Mobility of continental mantle: Evidence from postseismic geodetic observations following the 1992 Landers earthquake, *J. Geophys. Res.*, *105*(B4), 8035–8054, doi:10.1029/1999JB900380.
- Pollitz, F. F., R. Bürgmann, and W. Thatcher (2012), Illumination of rheological mantle heterogeneity by the M7.2 2010 El Mayor-Cucapah earthquake, *Geochem. Geophys. Geosyst.*, *13*, Q06002, doi:10.1029/2012GC004139.
- Rauch, H. E., F. Tung, and C. T. Striebel (1965), Maximum likelihood estimates of linear dynamic systems, *AIAA J.*, *3*(8), 1445–1450.
- Riva, R. E. M., and R. Govers (2009), Relating viscosities from postseismic relaxation to a realistic viscosity structure for the lithosphere, *Geophys. J. Int.*, *176*, 614–624, doi:10.1111/j.1365-246X.2008.04004.x.
- Rollins, C., S. Barbot, and J.-P. Avouac (2015), Postseismic deformation following the 2010 M7.2 El Mayor-Cucapah Earthquake: Observations, kinematic inversions, and dynamic models, *Pure Appl. Geophys.*, *172*(5), 1305–1358, doi:10.1007/s00024-014-1005-6.
- Savage, J. C. (1990), Equivalent strike-slip earthquake cycles in half-space and lithosphere-asthenosphere earth models, *J. Geophys. Res.*, *95*(B4), 4873–4879, doi:10.1029/JB095iB04p04873.
- Savage, J. C., and J. L. Svarc (2009), Postseismic relaxation following the 1992 M7.3 Landers and 1999 M7.1 Hector Mine earthquakes, southern California, *J. Geophys. Res.*, *114*, B01401, doi:10.1029/2008JB005938.
- Savage, J. C., J. L. Svarc, and S. B. Yu (2005), Postseismic relaxation and transient creep, *J. Geophys. Res.*, *110*, B11402, doi:10.1029/2005JB003687.
- Segall, P., and M. Mathews (1997), Time dependent inversion of geodetic data, *J. Geophys. Res.*, *102*(B10), 22,391–22,409.
- Spinler, J. C., R. A. Bennett, C. Walls, L. Shawn, and J. J. G. Garcia (2015), Assessing long-term postseismic deformation following the M7.2 4 April 2010, El Mayor-Cucapah earthquake with implications for lithospheric rheology in the Salton Trough, *J. Geophys. Res. Solid Earth*, *120*, 3664–3679, doi:10.1002/2014JB011613.
- Wei, M., D. Sandwell, Y. Fialko, and R. Bilham (2011), Slip on faults in the Imperial Valley triggered by the 4 April 2010 M_w 7.2 El Mayor-Cucapah earthquake revealed by InSAR, *Geophys. Res. Lett.*, *38*, L01308, doi:10.1029/2010GL045235.
- Wei, M., Y. Liu, Y. Kaneko, J. J. McGuire, and R. Bilham (2015), Dynamic triggering of creep events in the Salton Trough, Southern California by regional M5.4 earthquakes constrained by geodetic observations and numerical simulations, *Earth Planet. Sci. Lett.*, *427*, 1–10, doi:10.1016/j.epsl.2015.06.044.
- Wei, S., et al. (2011), Superficial simplicity of the 2010 El Mayor-Cucapah earthquake of Baja California in Mexico, *Nat. Geosci.*, *4*, 615–618, doi:10.1038/ngeo1213.
- Yang, M., and M. N. Toksöz (1981), Time-dependent deformation and stress relaxation after strike-slip earthquakes, *J. Geophys. Res.*, *86*, 2889–2901.
- Yuen, D. A., and W. R. Peltier (1982), Normal modes of the viscoelastic earth, *Geophys. J. R. Astron. Soc.*, *69*, 495–526, doi:10.1111/j.1365-246X.1982.tb04962.x.